OPTICA

Purcell-enhanced, directional light–matter interaction in a waveguide-coupled nanocavity

Nicholas J. Martin,[1,†,*] Dominic Hallett,[1,†] Mateusz Duda,[1] Luke Hallacy,[1] Elena Callus,[1] Luke Brunswick,[1] René Dost,[1] Edmund Clarke,[2] Pallavi K. Patil,[2] Pieter Kok,[1] Maurice S. Skolnick,[1] and Luke R. Wilson[1]

[1]School of Mathematical and Physical Sciences, University of Sheffield, Sheffield S3 7RH, UK
[2]EPSRC National Epitaxy Facility, University of Sheffield, Sheffield S1 4DE, UK
[†]These authors contributed equally.
*n.j.martin@sheffield.ac.uk

Received 11 March 2025; revised 24 June 2025; accepted 29 June 2025; published 14 July 2025

We demonstrate electrically tunable, spin-dependent, directional coupling of single photons by embedding quantum dots (QDs) in a waveguide-coupled nanocavity. The directional behavior arises from direction-dependent interference between two cavity modes when coupled to the device waveguides. The small-mode-volume cavity enables simultaneous Purcell enhancement (10.8 ± 0.7) and peak directional contrast ($88 \pm 1\%$), exceeding current state-of-the-art waveguide-only systems. We also present a scattering matrix model for the transmission through this structure, alongside a quantum trajectory-based model for predicting the system's directionality, which we use to explain the observed asymmetry in directional contrast seen in QD devices. Furthermore, the nanocavity enables wide-range electrical tuning of the emitter's directional contrast. We present results showing precise tuning of a QD emission line from a directional contrast of 2%–96%. In combination, these characteristics make this cavity–waveguide approach promising for use as a building block in directional nanophotonic circuits.

https://doi.org/10.1364/OPTICA.561630

1. INTRODUCTION

Achieving a high directional contrast alongside strong Purcell enhancement at the single-photon level has been a long-standing challenge in integrated quantum nanophotonics. Our novel nanocavity–waveguide system overcomes this barrier, advancing the potential for scalable quantum photonic technologies. Integrated nanophotonic systems have demonstrated the generation [1,2], manipulation [3–6], and detection [7,8] of quantum states in a scalable, on-chip architecture. For example, a highly effective two-way conduit for light and matter can be realized through the integration of an intrinsic quantum emitter (QE) within a nanophotonic waveguide supporting a single optical mode. Notable examples of such QEs include semiconductor quantum dots (QDs) [9], diamond color centers [10], and single atoms [6,11].

Enhanced light–matter interaction, quantified by the Purcell factor (F_P), offers transformative benefits for quantum photonic devices. These include increased photon indistinguishability, higher coupling efficiencies, and faster device operation rates, making it foundational for scalable quantum technologies [2,9,12–14]. By increasing the decay rate of a QE, the Purcell effect also reduces the impact of decoherence processes on the indistinguishability of emitted photons [13,15].

Directional nanophotonic devices harness the coupling between QE spin states and photon propagation directions. By engineering the device geometry to create regions of circularly polarized electric fields, these systems can selectively interface with spin-dependent transitions of QEs. This control facilitates functionalities such as spin-to-path conversion [16], path-dependent spin initialization [17], and proposals for entangling multiple QEs [18]. Additionally, the inherent nonreciprocity offers routes to compact optical circulators [19]. Although this spin-orbit coupling is frequently referred to as "chiral," since the emission direction depends on the handedness of the transition dipole moment, the underlying symmetry of both the waveguide geometry and the quantum dot structure remains unaltered.

Waveguide-based devices have made strides in achieving moderate Purcell factors ($3 < F_P < 5$) with robust directionality by embedding QEs in slow-light regions of photonic crystal waveguides. However, these designs struggle to combine high Purcell enhancement and directionality due to spatial polarization variations inherent in the waveguide field [20–23]. Although highly directional emission from a QD has been achieved in waveguide structures [21], the simultaneous combination of high directionality and large Purcell enhancement remains elusive, with the state-of-the-art being a Purcell factor of $F_P = 5 \pm 1$ for a chirally coupled QD [21].

This work demonstrates a novel cavity–waveguide system that achieves a record combination of high Purcell enhancement ($F_P = 10.8 \pm 0.7$) and high directional contrast ($C = 88 \pm 1\%$), alongside an electrically adjustable directionality from 2% to 96%. Unlike other approaches, our cavity–waveguide system can maintain a near-unity directional contrast even for emitter displacements up to 60 nm from the cavity center, offering unprecedented robustness to fabrication imperfections [24].

We develop theoretical models, including a scattering matrix model for transmission and a quantum trajectory-based model for directional contrast, to explain and predict the system's behavior. These models provide a deeper understanding of directionality and the interplay between system parameters, guiding the design of ideal quantum photonic devices. By combining theoretical rigor with experimental advancements, this work paves the way for scalable, tunable, and robust quantum photonic circuits, essential for future applications in quantum communications, computation, and sensing.

2. DEVICE STRUCTURE

As shown in Figs. 1(a) and 1(b), the device consists of a (170 nm thick) GaAs p-i-n membrane containing a layer of InAs QDs at its center. The membrane is patterned into a hexagonal-lattice photonic crystal with a period $a = 240$ nm and a hole radius $r = 0.3a$, creating a photonic bandgap for TE-polarized light spanning 730−1050 nm. AlGaAs tunneling barriers on either side of the QD layer help confine charge carriers, whereas the top p-doped and bottom n-doped layers enable Stark tuning of the QD emission wavelength via an applied bias.

By omitting an air hole in the center, we form an H1 cavity. Removing a row of holes on opposite sides of the cavity creates two W1 waveguides, which couple to the cavity modes and guide light toward nanobeam waveguides and outcoupler gratings for efficient off-chip collection. The inner holes of the H1 cavity are reduced to a radius $r_c = 0.21a$ and displaced outward by $0.09a$, while the inner holes of the W1 waveguides are reduced to a radius $r_w = 0.27a$. These adjustments allow for precise control of the cavity mode frequencies and coupling properties. Figure 1(c) shows a scanning electron microscope (SEM) image of the fabricated structure, overlaid with the simulated time-averaged electric field intensity, illustrating the mode profiles for (i) a σ^- dipole and (ii) a σ^+ dipole placed in the center of the cavity. Additional details on the sample are provided in Section S5 in Supplement 1.

3. THEORY

To accurately capture the behavior of the device, our theory must account for realistic QD properties, including fine-structure splitting, imperfect crystalline symmetry, and dipole misalignment. These factors lead to deviations from ideal circular polarization and coherent population transfer between the QD's excited states. A simple two-level model of a perfectly aligned, circularly polarized emitter cannot reproduce the asymmetric directional emission that we observed in our experiments. By including a three-level QD structure, complex coupling rates, and the associated interference effects, our model provides a faithful representation of the QD–cavity–waveguide system.

In this section, we provide an overview of the theoretical models used to describe the waveguide-coupled nanocavity system and to predict the device's performance. We present the key equations below; more details are provided in the appendices, with detailed derivations given in Supplement 1.

As shown in Fig. 2, we consider a QD with fine-structure splitting, modeled as a three-level V-type emitter $\{|g\rangle, |e_1\rangle, |e_2\rangle\}$, coupled to two orthogonal cavity modes $\{H, V\}$, and further

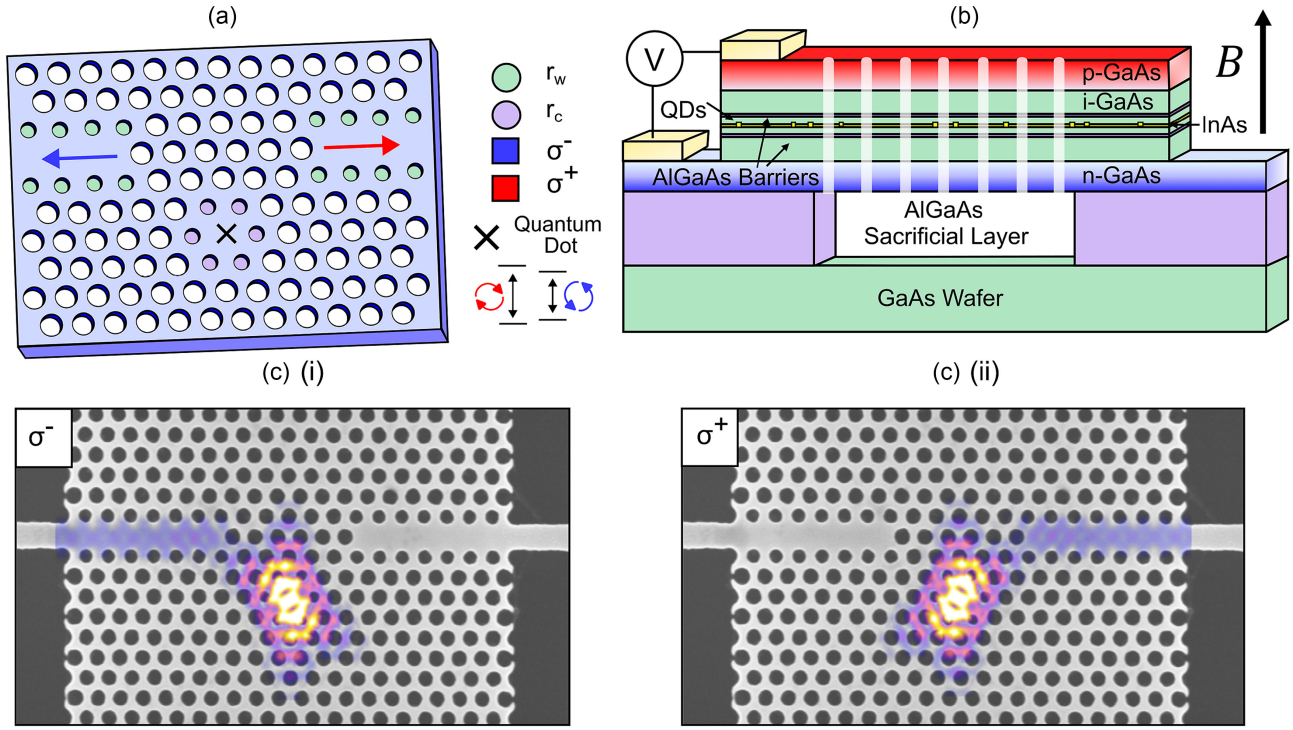

Fig. 1. (a) Schematic of the cavity design. (b) Stack diagram showing the structure of the QD wafer. (c) An SEM image of the photonic crystal device overlaid with the time-averaged electric field intensity for the device with (i) a σ^- dipole and (ii) a σ^+ dipole at the center of the cavity.

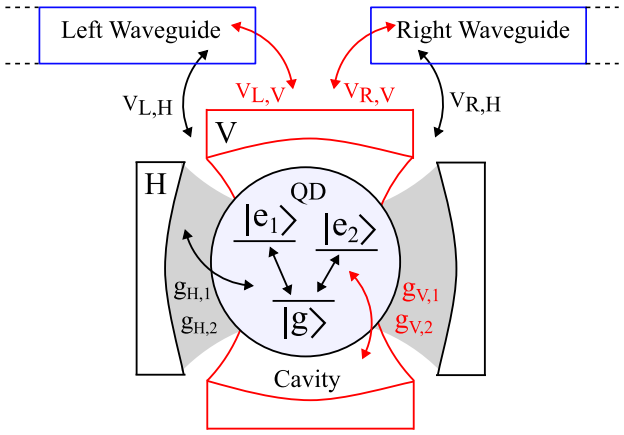

Fig. 2. Schematic of the waveguide-coupled nanocavity. Transition $j \in \{1, 2\}$ of the QD ($|g\rangle \leftrightarrow |e_j\rangle$) has frequency $\omega_{e,j}$ and couples to the cavity mode $\alpha \in \{H, V\}$ (having resonance frequency $\omega_{c,\alpha}$) with the coupling rate $g_{\alpha,j}$. The cavity mode α also couples to the right and left waveguides with coupling rates $V_{R,\alpha}$ and $V_{L,\alpha}$, respectively.

coupled to the left (L) and right (R) waveguides. The frequency of the $|g\rangle \leftrightarrow |e_j\rangle$ transition is $\omega_{e,j}$ and the emitter–cavity coupling rates are denoted by $g_{\alpha,j}$, where $j \in \{1, 2\}$ labels the QD transitions and $\alpha \in \{H, V\}$ labels the two cavity modes. The mode frequency of the H (V) mode is $\omega_{c,H}$ ($\omega_{c,V}$). Furthermore, the cavity–waveguide coupling rates are $V_{\mu,\alpha}$, where $\mu \in \{L, R\}$ labels the left and right waveguides, respectively. The cavity modes are coupled to the two waveguides with equal strength, so we calculate these coupling rates as $V_{R,\alpha} = V_{L,\alpha} = \omega_{c,\alpha}/2Q_\alpha$, where Q_α is the quality (Q) factor of mode α.

The total Hamiltonian for the system takes the following form:

$$H = H_e + H_c + H_{wg} + H_{e\text{-}c} + H_{c\text{-}wg}, \tag{1}$$

where the emitter Hamiltonian H_e, the cavity Hamiltonian H_c, the waveguide Hamiltonian H_{wg}, the emitter–cavity interaction $H_{e\text{-}c}$, and the cavity–waveguide interaction $H_{c\text{-}wg}$ are given in Appendix A. Using the input–output formalism [25,26], we derive the single-photon scattering matrix elements for the waveguide-to-waveguide transmission, e.g.,

$$S_{pk}^{RL} = t_{RL}\delta(p - k), \tag{2}$$

where k and p denote the input and output photon frequencies, respectively, and t_{RL} is the transmission coefficient for left-to-right transmission (see Appendix B and Section S1 in Supplement 1 for the derivation and result). From this, we obtain the transmission probability $|t_{RL}|^2$ and use it to fit experimental data from our transmission measurements.

To predict the directional contrast of the system, we use a space-discretized waveguide model based on quantum trajectory theory [27–29], which allows us to simulate the time evolution of the system and calculate the probability of a photon being emitted into each of the waveguides. In the model, each waveguide is discretized into a series of N boxes. At each time step in the quantum trajectory algorithm, the cavity interacts with the first box in each waveguide (box 0), photon number measurements are simulated on the final box in each waveguide (box $N-1$), the quantum state of the system is projected according to the measurement results, and the boxes are moved along by one (see Appendix C and Section S2 in Supplement 1 for more details). Each trajectory is a stochastic evolution process, so we take an average over many trajectories to compute the expected time evolution of observables (conditioned on photon detection events at the waveguide ends). The directional contrast C is then given by the normalized difference between the final waveguide box populations at the end of the trajectories (i.e., at time $t = t_{end}$):

$$C = \left| \frac{\langle A_{R,N-1}^\dagger A_{R,N-1}\rangle_{t=t_{end}} - \langle A_{L,N-1}^\dagger A_{L,N-1}\rangle_{t=t_{end}}}{\langle A_{R,N-1}^\dagger A_{R,N-1}\rangle_{t=t_{end}} + \langle A_{L,N-1}^\dagger A_{L,N-1}\rangle_{t=t_{end}}} \right|, \tag{3}$$

where $A_{\mu,N-1}$ ($A_{\mu,N-1}^\dagger$) is the annihilation (creation) operator for the final box of waveguide μ (box $N-1$). The end time t_{end} is chosen such that the emitter has fully decayed to its ground state $|g\rangle$ by the end of the simulations, and all of the photon population has been transferred to the ends of the waveguides. Equation (3) allows us to predict the directional contrast of our system for a given initial state and chosen parameters, and therefore to study how the energy level structure of the QD and the coupling rates affect the degree of directionality.

From our experimental results, we can extract the contrast using the relative power transmitted through the waveguides when exciting the QD in the cavity:

$$C = \left| \frac{P_R - P_L}{P_R + P_L} \right|, \tag{4}$$

where P_R (P_L) is the power transmitted to the right (left). This enables us to quantify the directional performance of our device and to compare the experimental results with theoretical predictions from the quantum trajectory model.

4. RESULTS

Due to the random positioning of the self-assembled QDs used in this work, the occurrence of directional coupling is probabilistic. In this section, we present results for two devices (labeled Device 1 and Device 2), where a demonstration of the design's wavelength-dependent directionality and Purcell enhancement properties is shown.

A. Device 1: Quantum Dots with Simultaneous High Enhancement and Directional Contrast

Achieving both large Purcell enhancement and highly directional emission in solid-state QEs has been a longstanding challenge. Here, Device 1 overcomes this, demonstrating a directional contrast of $C = 88 \pm 1\%$ and a Purcell factor of $F_P = 10.8 \pm 0.7$.

The mode properties of the cavity are measured by exciting a broad ensemble of QDs in and around the cavity using an 808 nm laser and collecting photoluminescence (PL) from one outcoupler. The intensity of PL as a function of wavelength for Device 1 is shown in Fig. 3(a). By fitting the data with a Lorentzian function, we extract a resonant wavelength of 946.63 nm (948.93 nm) and a Q factor of 810 (320) for the H (V) mode, respectively. From these Q factors and resonant wavelengths, we are able to predict the maximum directional contrast possible for a circularly polarized emitter at the cavity center using the trajectories model, as well as the expected transmission from the scattering matrix model, as shown in Figs. 4(c) and 3(b) respectively. The transmission data presented in Fig. 3(b) is obtained by exciting one outcoupler of the device with a laser to excite a broad QD ensemble and measuring the PL intensity at the opposite outcoupler. This experimental

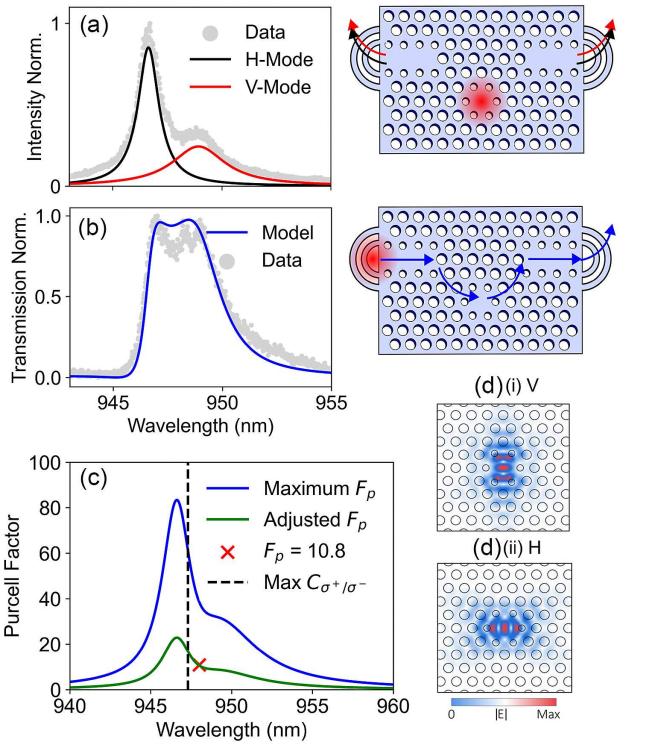

Fig. 3. (a) Measurement of the cavity modes of Device 1, with the fits to the data being two Lorentzian peaks. (b) Measured waveguide-to-waveguide transmission through Device 1, fit using our scattering matrix model. (c) Purcell factor as a function of wavelength for Device 1. The blue curve represents the calculated maximum Purcell factor F_p, while the green curve shows the adjusted Purcell factor accounting for the QD's offset position and non-resonant excitation, calculated from the experimentally measured result. The red cross highlights the measured Purcell factor of $F_p = 10.8$ at 948 nm. The dashed vertical line at 947.3 nm indicates the wavelength where the directional contrast is predicted to peak at 98%, with the corresponding Purcell enhancement estimated to be 16.8. (d) The electric field profiles of the (i) V and (ii) H cavity modes. Regions of higher electric field concentration correspond to a greater Purcell enhancement.

result is compared with the expected transmission for a device with these cavity mode properties, as predicted by our transmission model. Figure 3(c) shows the expected maximum Purcell factor in the center of the cavity for a circularly polarized emitter, modeled based on the mode data presented in Fig. 3(a) (see Appendix D). Figure 3(d) illustrates the electric field profiles of cavity modes (i) V and (ii) H, where regions of higher electric field concentration correspond to greater Purcell enhancement, with the maximum enhancement occurring in the center of the cavity.

Figure 4(b)(i–ii) shows the magnetic field dependence (ranging from −5 to 5 T) of PL emission from the QD in Device 1, collected from the two outcouplers. The directional behavior of this emission is clearly visible across the magnetic field range, as the applied magnetic field creates well-resolved σ^+ and σ^- dipoles. Figure 4(a)(i–ii) shows the individual spectra for −5 T, where it can clearly be seen that the emission of the σ^+ state is predominantly to the right outcoupler, while the emission of the σ^- state couples predominantly to the left outcoupler. In Fig. 4(c), the experimentally measured directional contrast is plotted as a function of the QD emission wavelength (crosses), which was controlled by tuning the applied magnetic field strength. The magnetic field is capable of tuning the QD wavelength over a range of 0.63 nm, from 947.87 to 948.5 nm. In the figure, the measured directional contrast is compared to what is expected for a device with the measured mode properties (black curve). We see that the measured lower contrast at longer wavelengths matches our trajectory model for the wavelength dependence of the contrast.

Figure 4(d) shows a measurement of the QD decay time. In this measurement, the QD is excited with an fs laser pulse at 810 nm. The QD transition at 948.0 nm exhibits a decay time $\tau_0 = (104 \pm 2)$ ps within an applied magnetic field of $B = 2$T. The instrument response function is a Gaussian with a full width at half-maximum of 50 ps. From measurements of the decay time for 10 QDs in bulk GaAs in this sample, we extract an average ensemble lifetime of $\tau_{\text{bulk}} = (1.13 \pm 0.08)$ ns, and therefore estimate the Purcell factor of the QD in the cavity to be $F_P = \tau_{\text{bulk}}/\tau_0 = 10.8 \pm 0.7$. We note that the QD lifetime was measured using above-band excitation, which introduces a contribution to the decay time from inter-band processes. Since the QD was not visible under resonant excitation, we were unable to directly measure the resonant decay time. Therefore, the measured value represents only a lower bound for the true Purcell factor. Moreover, in this device, it was not possible to tune the QD to shorter wavelengths. At 947.3 nm, where the directional contrast is predicted to peak at 98%, the Purcell enhancement using an above-band excitation scheme is predicted to be 16.8, as determined from Eq. (D1) in Appendix D.

B. Device 2: Quantum Dots with Highly Tunable Asymmetric Directional Contrast

Figure 5 summarizes the experimental results from Device 2. In this device, the QDs exhibited longer decay times and could be tuned over a wavelength range of approximately 1.75 nm, making them ideal for studying and controlling the directional contrast. Figure 5(b) displays the cavity modes, with resonant wavelengths of 930.9 nm for the H mode and 933.6 nm for the V mode, and corresponding Q factors of 660 and 779. Based on the absence of a significant Purcell enhancement in this device, we believe that the QD is offset from the cavity center, leading to unequal coupling to the H and V modes due to the spatial variation in the cavity field profiles. The measured transmission through the device, shown in Fig. 5(c), agrees well with the predictions of our transmission model.

Figure 5(a)(i–ii) shows the PL spectra of a QD transition collected from the left and right outcouplers under varying applied voltages and a 1.5 T magnetic field. The magnetic field induces Zeeman splitting, resulting in two distinct components labeled as σ^+ and σ^-. The PL spectra show how the emission intensities for each Zeeman component shift as the applied voltage varies between −4 and 0.5 V. In Fig. 5(a)(i), the normalized PL intensities collected from the left outcoupler reveal that the relative strength of the σ^+ and σ^- transitions depends strongly on the applied bias. Similarly, Fig. 5(a)(ii) demonstrates this voltage-dependent behavior in the PL spectra collected from the right outcoupler, with complementary changes in intensity.

By normalizing the PL spectra from the left and right outcouplers and applying Eq. (4), we compute the wavelength-dependent directional contrast, which is shown in Fig. 5(d). For the emission line corresponding to σ^+, the directional contrast can be dynamically tuned from 2% to 96%. This significant tunability is achieved through the quantum-confined Stark effect, where the applied bias alters the QD's energy levels, shifting the emission

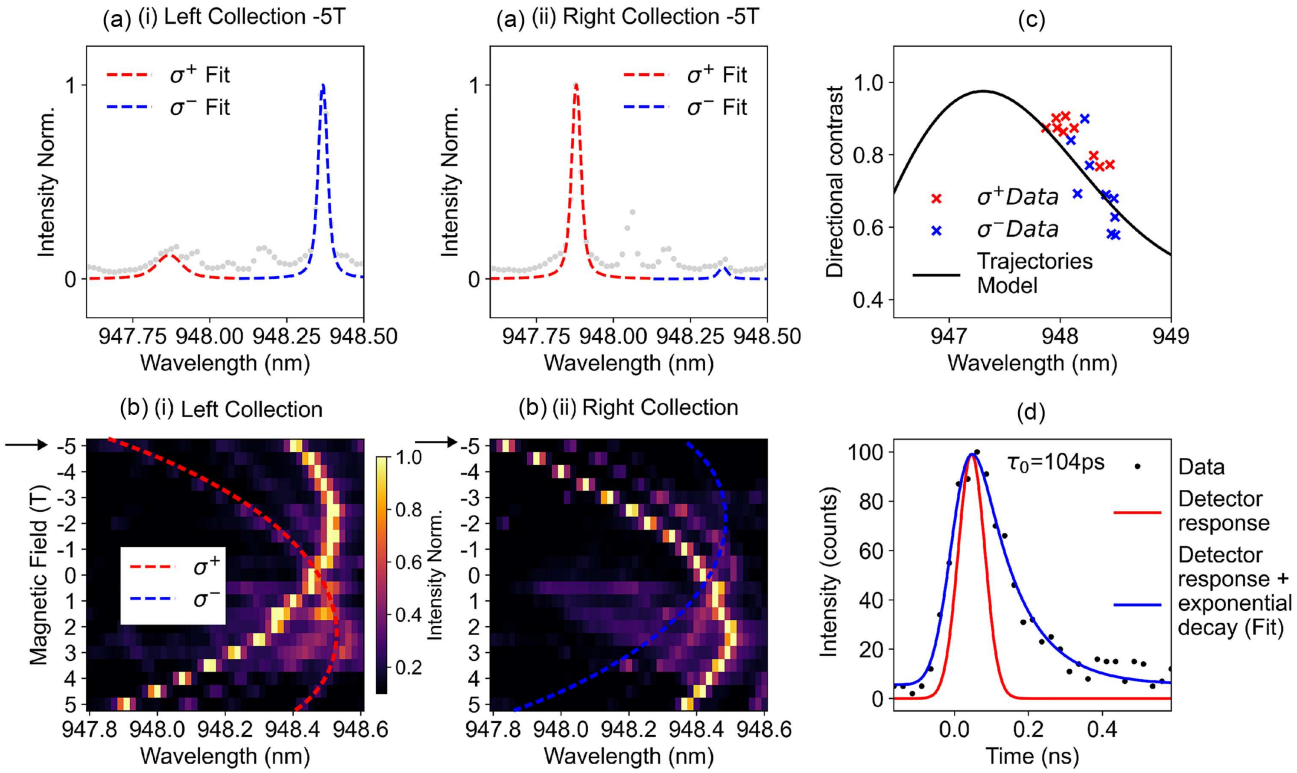

Fig. 4. (a) PL spectra, exciting the cavity, collected from the (i) left and (ii) right outcouplers, with an applied magnetic field $B = -5$ T. The Zeeman-split emission lines of the QD are fit using Voigt functions. (b) Magnetic field dependence of PL emission from the QD, measured from the (i) left and (ii) right outcouplers. The dashed lines mark the wavelengths of the two QD spin states. (c) Directional contrast of a charged exciton state of the QD in Device 1, as a function of the wavelength. The QD emission wavelength was tuned through the application of a magnetic field from −5 to 5 T in a Faraday geometry. The prediction of the directional contrast for a circularly polarized emitter from the quantum trajectory model (black curve) is presented in comparison to the measured data (crosses). (d) Measurement of the QD decay time. The instrument response function is indicated by a red line, and the blue fit is an exponential decay convolved with the instrument response.

wavelength and modulating the contrast. The ability to electrically tune the directional contrast provides precise control over the optical properties of the device, making it highly suitable for dynamic photonic applications such as tunable optical isolators or directional emitters.

However, the observed directional contrast in Fig. 5(d) deviates significantly from the predictions of the contrast based solely on the degree of circular polarization (DCP) of the electric field in the cavity [24] (dashed curves). A striking feature in Device 2 is the asymmetry in contrast between the Zeeman components of the QD states, an effect that finite-difference time-domain (FDTD) simulations and a simple DCP analysis do not predict. This clear discrepancy underscores the limitations of the DCP model in capturing complex emitter–cavity interactions and directional asymmetries. Similar asymmetries have been reported in previous studies [3,16,30–32].

To resolve this, our quantum trajectory model, unlike the DCP approach, allows us to consider different emitter–cavity coupling rates, which can generally deviate from ideal circular polarization. For example, the QD can couple to the cavity modes H and V with different strengths due to having different spectral or spatial overlap with the two modes, and the phase difference in the coupling to H and V can deviate from $\pi/2$ (which is the phase required for circular polarization and assumed by the DCP model) due to dipole misalignment. By including general emitter–cavity coupling rates, the model successfully reproduces the experimentally observed asymmetry, demonstrating its predictive capability and highlighting its ability to capture the complex physics behind wavelength-dependent directional contrast.

As shown in Fig. 3(d), the cavity modes H and V exhibit distinct regions of electric field concentration. Near the center of the cavity, the emitter experiences symmetric coupling to both modes, minimizing mismatch. However, displacements greater than 60 nm from the center introduce significant spatial mismatches, thus altering the Purcell factors for the H and V modes. Hence, unequal coupling to the modes can be expected in this regime. Another consideration, also mentioned above and accounted for in the quantum trajectory model, is that misalignment of the emitter from the crystal axis will alter its intrinsic dipole orientation relative to the cavity field, causing the emitted photons to acquire mixed or elliptical polarization states rather than pure circular σ^+/σ^- polarizations. This mixing changes how the emitter couples to the cavity modes and can affect both the coupling efficiencies and the resulting directional emission characteristics. Additionally, deviations from ideal dot symmetry can further modify the polarization states and coupling rates. In Fig. 5(d), the solid orange and blue lines represent the contrast predicted by our quantum trajectory model, aligning closely with the experimental asymmetry observed in Fig. 5(a)(i–ii). A more detailed discussion of these dynamics and the coupling rate parameters used in this figure is provided in Sections S3 and S6 in Supplement 1.

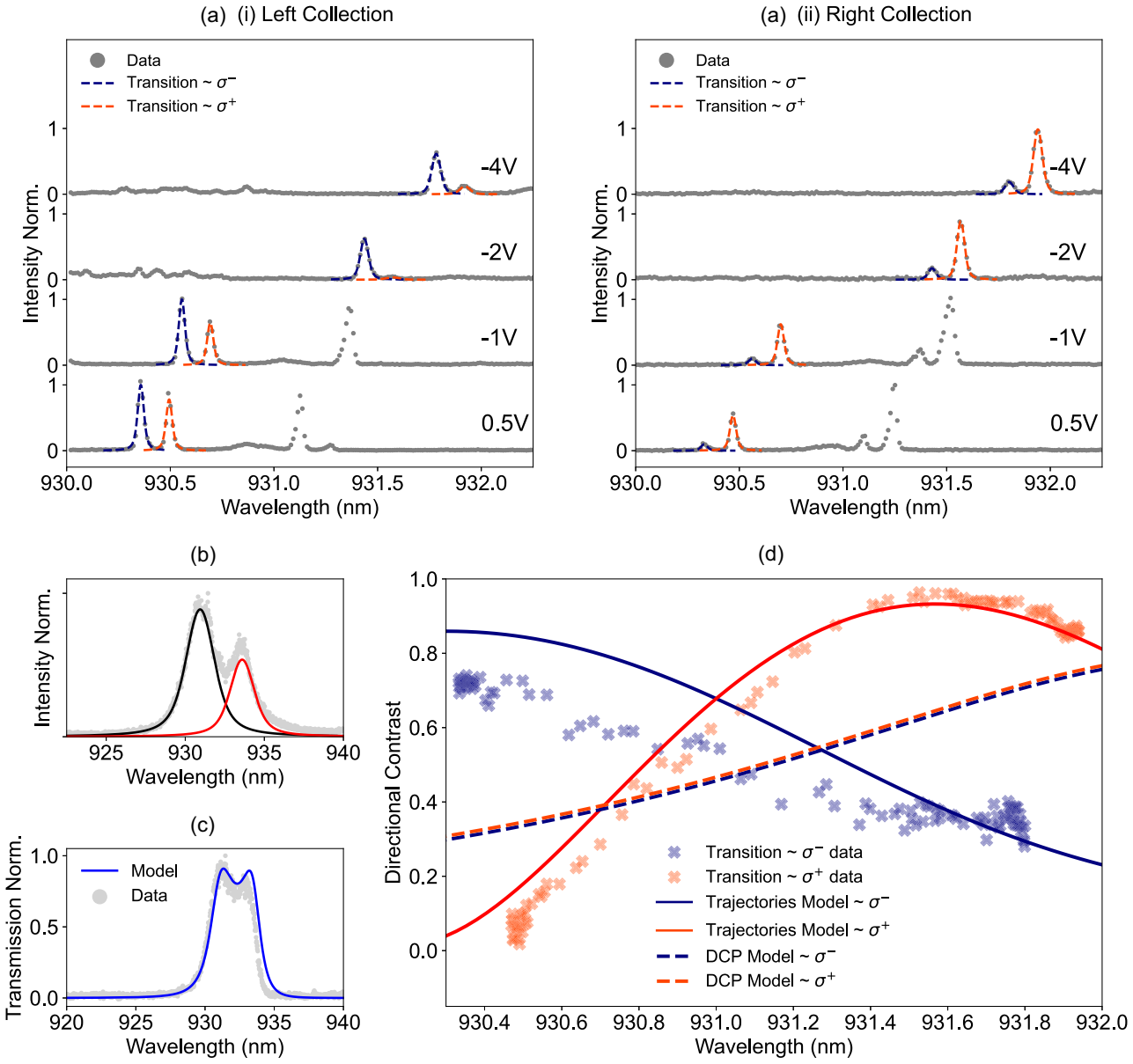

Fig. 5. (a) Individual PL spectra at −4, −2, −1, and 0.5 V for collection from the (i) left and (ii) right outcouplers, showing the individual QD emission lines. The QD lines are fit using a Voigt function. (b) Measurement of the H1 cavity modes of Device 2 through the same method as Fig. 3(a); the data are fit by two Lorentzian peaks. (c) Measured waveguide-to-waveguide transmission through Device 2, fit using our transmission model. (d) Directional contrast for Device 2 as a function of the emitter wavelength. The contrast is measured for the Zeeman-split lines of a QD within a 1.5 T magnetic field. The data are compared with predictions from the quantum trajectory model (solid curves), as well as with the DCP at the cavity center (dashed curves), which is the contrast expected for a circularly polarized emitter [24].

5. CONCLUSION

In conclusion, our work has successfully demonstrated a waveguide-coupled cavity nanophotonic device that achieves a remarkable balance between near-unity directional coupling and significant Purcell enhancement for an embedded circularly polarized emitter. The low mode volume of the H1 cavity, approximately $V \approx 0.6(\lambda/n)^3$ [33], is critical in achieving a large emitter–cavity coupling strength within a relatively low-Q ($Q \approx 400-1000$) cavity environment. The performance of the device is robust against both spectral and spatial perturbations of the embedded emitter, a significant advancement over alternative approaches [24]. In particular, as shown in [24], the directional contrast of our device remains exceptionally high even with emitter displacements up to 60 nm from the center of the cavity. This feature underlines the potential of the device in applications where precise emitter positioning can be challenging. This spatial robustness makes this cavity design highly compatible with preselection methods such as wide-field photoluminescence mapping [34], which enables devices to be fabricated around registered QDs. This facilitates optimal spatial and spectral overlap with the cavity modes and can significantly improve device yield, addressing a common challenge associated with randomly positioned self-assembled QDs.

Furthermore, our experiments on two devices reveal that the directional contrast strongly depends on the wavelengths of the cavity modes and the emitter. This sensitivity allows

post-fabrication tuning and optimization [35], demonstrating the device's adaptability to varying emitter properties while maintaining high performance. We present results showing precise tuning of a QD emission line from a directional contrast of 2%–96%. Notably, our quantum trajectory model explains for the first time the observed asymmetry in directional contrast seen in QD devices and provides a clear pathway for optimizing QD-based directional light–matter interfaces, even in the presence of imperfect polarization. Recently, another numerical framework for simulating waveguide QED systems was proposed [36], which can further support the study of such devices with a reduced computation time compared to the quantum trajectory approach.

Lastly, the general mechanism behind our directional light–matter interaction is not confined to our specific cavity design. It extends to other cavity architectures that support degenerate orthogonal modes, such as micropillars [37], and would be effective for systems operating in the telecom bands [38,39]. This broad applicability could pave the way for a range of high-performance applications in quantum nanophotonics, including reconfigurable phase shifters [40], quantum routers and switches [41], and compact optical circulators [19].

In this Appendix, we present details of our theoretical models that are relevant to the discussions in the main text. More detailed calculations are contained in Supplement 1.

APPENDIX A: SYSTEM HAMILTONIAN

We consider the system depicted in Fig. 2 in the main text. In Eq. (1), we have the free emitter Hamiltonian ($\hbar = 1$):

$$H_e = \sum_{j=1,2} \omega_{e,j} \sigma_j^+ \sigma_j^-, \tag{A1}$$

where $\sigma_j^+ = |e_j\rangle\langle g|$ and $\sigma_j^- = |g\rangle\langle e_j|$ are the raising and lowering operators for transition $j \in \{1, 2\}$. The free cavity Hamiltonian is

$$H_c = \sum_{\alpha=H,V} \omega_{c,\alpha} c_\alpha^\dagger c_\alpha, \tag{A2}$$

where c_α and $c_\alpha^\dagger$ are the annihilation and creation operators for mode $\alpha \in \{H, V\}$, and the free waveguide Hamiltonian is

$$H_{\mathrm{wg}} = \sum_{\mu=L,R} \int \omega(k) a_\mu^\dagger(k) a_\mu(k) \mathrm{d}k, \tag{A3}$$

where the operators $a_\mu(k)$ and $a_\mu^\dagger(k)$ annihilate and create photons with the wave number k in the waveguide $\mu \in \{L, R\}$. This Hamiltonian assumes identical dispersion relations $\omega(k)$ for both waveguides.

The emitter–cavity interaction is of the Jaynes–Cummings form:

$$H_{\mathrm{e\text{-}c}} = \sum_{j=1,2} \sum_{\alpha=H,V} \left(g_{\alpha,j} \sigma_j^+ c_\alpha + g_{\alpha,j}^* \sigma_j^- c_\alpha^\dagger \right), \tag{A4}$$

and the cavity–waveguide interaction, under the Markov approximation [25] (assuming coupling independent of k), is

$$H_{c-\mathrm{wg}} = \sum_{\alpha=H,V} \sum_{\mu=L,R} \int \left[\sqrt{\frac{V_{\mu,\alpha}}{2\pi}} a_\mu^\dagger(k) c_\alpha e^{i\pi\delta_{\alpha H}\delta_{\mu L}} + \sqrt{\frac{V_{\mu,\alpha}^*}{2\pi}} a_\mu(k) c_\alpha^\dagger e^{-i\pi\delta_{\alpha H}\delta_{\mu L}} \right] \mathrm{d}k. \tag{A5}$$

The phase factors $e^{\pm i\pi\delta_{\alpha H}\delta_{\mu L}}$ reflect the anti-symmetric coupling of the cavity modes into the left and right waveguides, which gives rise to the interference that enables directional emission in our device [24].

APPENDIX B: SCATTERING MATRIX MODEL

The single-photon scattering matrix elements are given by

$$S_{pk}^{\mu\nu} = \langle p_\mu | S | k_\nu \rangle = \langle p_\mu^- | k_\nu^+ \rangle = \langle 0 | a_{\mu,\mathrm{out}}(p) a_{\nu,\mathrm{in}}^\dagger(k) | 0 \rangle, \tag{B1}$$

where k is the frequency of the input photon in the waveguide ν, p is the frequency of the output photon in the waveguide μ, $|k_\nu^+\rangle = a_{\nu,\mathrm{in}}^\dagger(k)|0\rangle$ and $|p_\mu^-\rangle = a_{\mu,\mathrm{out}}^\dagger(p)|0\rangle$ are scattering eigenstates, and $|0\rangle$ is the vacuum state of the system. For transmission, we set $\mu \neq \nu$, such that the output photon leaves in the opposite waveguide to the input photon. For example, for left-to-right transmission, $\nu = L$ and $\mu = R$, and the corresponding transmission matrix element has the form

$$S_{pk}^{RL} = \langle 0 | a_{R,\mathrm{out}}(p) a_{L,\mathrm{in}}^\dagger(k) | 0 \rangle = t_{RL} \delta(p - k), \tag{B2}$$

where t_{RL} is the transmission coefficient, and $\delta(p - k)$ enforces energy conservation. The derivation of the scattering matrix is presented in Section S1 in Supplement 1, where we obtain the transmission coefficient for both left-to-right and right-to-left propagation and demonstrate that the directional light–matter interaction in our cavity can give rise to nonreciprocal phase shifts.

APPENDIX C: QUANTUM TRAJECTORY MODEL

In the quantum trajectory model, each waveguide is discretized into a series of N spatial bins of width Δt in time (labeled with the index $n \in \{0, 1, \ldots, N-1\}$), allowing the time evolution to be solved numerically in discrete time steps. In Section S2 in Supplement 1, we discretize the Hamiltonian from Eq. (1) (with the terms defined in Appendix A), where we replace the continuum waveguide mode operators $a_\mu(k)$, $a_\mu^\dagger(k)$ with discrete mode operators $a_{\mu,k}$, $a_{\mu,k}^\dagger$, and use the discrete Fourier transforms:

$$A_{R,n} = \frac{1}{\sqrt{N}} \sum_{k=0}^{N-1} a_{R,k} e^{i\omega_k n \Delta t} \tag{C1}$$

and

$$A_{L,n} = \frac{1}{\sqrt{N}} \sum_{k=0}^{N-1} a_{L,k} e^{-i\omega_k n \Delta t} \tag{C2}$$

to transform from the k-space to the position space (ω_k is the discretized waveguide dispersion relation). The operator $A_{\mu,n}$ ($A_{\mu,n}^\dagger$) annihilates (creates) a photon in the spatial bin n of the waveguide μ. After discretizing the Hamiltonian, we express all operators as matrices by choosing the following basis consisting of states with at most one photon in the system (since we consider single-photon emission from the cavity):

$$\{|g, 0_H, 0_V, 0_{R,N-1}, \ldots, 0_{R,0}, 0_{L,N-1}, \ldots, 0_{L,0}\rangle,$$
$$|e_1, 0_H, 0_V, 0_{R,N-1}, \ldots, 0_{R,0}, 0_{L,N-1}, \ldots, 0_{L,0}\rangle,$$
$$|e_2, 0_H, 0_V, 0_{R,N-1}, \ldots, 0_{R,0}, 0_{L,N-1}, \ldots, 0_{L,0}\rangle,$$
$$|g, 1_H, 0_V, 0_{R,N-1}, \ldots, 0_{R,0}, 0_{L,N-1}, \ldots, 0_{L,0}\rangle,$$
$$|g, 0_H, 1_V, 0_{R,N-1}, \ldots, 0_{R,0}, 0_{L,N-1}, \ldots, 0_{L,0}\rangle,$$
$$|g, 0_H, 0_V, 1_{R,N-1}, \ldots, 0_{R,0}, 0_{L,N-1}, \ldots, 0_{L,0}\rangle,$$
$$\vdots$$
$$|g, 0_H, 0_V, 0_{R,N-1}, \ldots, 0_{R,0}, 0_{L,N-1}, \ldots, 1_{L,0}\rangle\}. \quad \text{(C3)}$$

The basis states are tensor products of states from the emitter basis, the cavity basis, and the discrete position-space waveguide basis, where $|0_\alpha\rangle$ ($|1_\alpha\rangle$) corresponds to no photons (one photon) in the cavity mode α, and $|0_{\mu,n}\rangle$ ($|1_{\mu,n}\rangle$) corresponds to no photons (one photon) in the spatial bin n in the waveguide μ.

At the start of each trajectory simulation, we set the emitter to be in a superposition of its excited states $|e_1\rangle$ and $|e_2\rangle$ and observe how the population of the excited states decays into the waveguides as the system evolves in time. The initial state $|\psi(0)\rangle$ is therefore written in our basis as

$$|\psi(0)\rangle = \alpha|e_1, 0_H, 0_V, 0_{R,N-1}, \ldots, 0_{L,0}\rangle + \beta|e_2, 0_H, 0_V, 0_{R,N-1}, \ldots, 0_{L,0}\rangle, \quad \text{(C4)}$$

with the normalization condition $|\alpha|^2 + |\beta|^2 = 1$.

The data presented for Device 1 correspond to a charged exciton QD state. Here, we model one Zeeman component of the QD as a two-level system with the initial condition $\alpha = 1$, $\beta = 0$, and with emitter–cavity coupling rates $g_{H,1}/2\pi = 10$ GHz and $g_{V,1}/2\pi = 10e^{i\pi/2}$ GHz ($g_{H,2} = g_{V,2} = 0$), corresponding to circular polarization. Note that $g_{V,1}/2\pi = 10e^{-i\pi/2}$ GHz can equivalently be used, as the contrast is symmetric for the two circular Zeeman components σ^+/σ^- (as in the DCP model). The results for Device 2 correspond to a neutral exciton, so in this case we model each Zeeman component as a three-level system (with fine structure splitting) and initial condition $\alpha = \beta = 1/\sqrt{2}$, where we assume that the two fine-structure states are populated equally during non-resonant excitation. The emitter–cavity coupling rates $g_{\alpha,j}$ are also modified to account for unequal coupling to the H and V modes and phase differences resulting from dipole misalignment, which explains the asymmetric contrast in Fig. 5(d).

At each time step in the quantum trajectory algorithm, the cavity interacts with the first box ($n = 0$) in each waveguide, photon number measurements are simulated on the final waveguide boxes ($n = N - 1$), and the boxes are moved along by one (see Supplement 1 for more details). In order to obtain the directional contrast C in Eq. (3) in the main text, we calculate the expectation values:

$$\langle A^\dagger_{\mu,N-1} A_{\mu,N-1}\rangle = \langle\psi(t)|A^\dagger_{\mu,N-1} A_{\mu,N-1}|\psi(t)\rangle, \quad \text{(C5)}$$

for $\mu \in \{L, R\}$ at each time step, which are the populations of the final waveguide boxes. From these, we calculate C at the end of the trajectories ($t = t_{\text{end}}$), once the emitter has fully decayed and all the photon population has reached the ends of the waveguides.

Note that the quantum trajectory model assumes that the system is in a pure state at all times. This is a simplified description, as in general we expect above-band non-resonant excitation to form a mixed state of $|e_1\rangle$ and $|e_2\rangle$, as opposed to a coherent superposition. Nevertheless, Fig. 5(d) shows that the pure state description gives a good approximation to the directional contrast measured in our experiments. We believe this model is sufficient for our system, without requiring a more sophisticated mixed-state treatment, as the measurements were performed in a regime where the Zeeman splitting is much larger than the fine structure splitting, in which case the coherence (or lack thereof) between the fine-structure states is insignificant. Even though the magnitude of the fine structure splitting alone does not affect the contrast in this regime, the inclusion of fine structure leads to the possibility of having different emitter–cavity coupling rates for the two transitions, which modifies the contrast (see Section S3 in Supplement 1).

APPENDIX D: PURCELL ENHANCEMENT

Considering the two modes of our cavity system, a circularly polarized emitter will emit into the modes as a proportion of the Purcell factor of that mode ($\alpha \in \{H, V\}$):

$$f_\alpha = \frac{F_\alpha}{F_H + F_V}. \quad \text{(D1)}$$

The total Purcell factor for a circularly polarized emitter in the cavity is given by

$$F_{\text{tot}} = \frac{F_H^2 + F_V^2}{F_H + F_V}, \quad \text{(D2)}$$

for $\alpha \in \{H, V\}$,

$$F_\alpha = \frac{3Q_\alpha}{4\pi^2 V_\alpha} \frac{(2\kappa_\alpha)^2}{4(\omega_e - \omega_{c,\alpha})^2 + (2\kappa_\alpha)^2} \frac{|\boldsymbol{\mu}\cdot\mathbf{E}(\mathrm{r}_0)|^2}{|\boldsymbol{\mu}|^2|\mathbf{E}_{\max}|^2}. \quad \text{(D3)}$$

Here, Q_α is the Q factor of the cavity mode α, and V_α is the mode volume in cubic wavelengths. In addition, ω_e is the emitter transition frequency, $\omega_{c,\alpha}$ is the mode frequency of the cavity mode α, and $2\kappa_\alpha$ is the full width at half-maximum of the cavity mode. Furthermore, $\boldsymbol{\mu}$, $\mathbf{E}(\mathrm{r}_0)$, and $\mathbf{E}_{\max}$ are the transition dipole moment, electric field at the emitter's position, and the maximum electric field in the cavity, respectively.

Funding. Engineering and Physical Sciences Research Council (EP/N031776/1, EP/W524360/1, EP/R513313/1, EP/V026496/1).

Acknowledgment. The authors acknowledge helpful discussions with Mahmoud Jalali Mehrabad, Yuxin Wang, and Matias Bundgaard-Nielsen. This work was supported by EPSRC Grant No. EP/N031776/1, EP/W524360/1, EP/R513313/1, and EP/V026496/1.

D.H. designed the photonic structures, which R.D. fabricated. N.J.M., D.H., L.H., L.B., and M.D. carried out the measurements and simulations. E.C. and M.D. developed the scattering matrix model for transmission. M.D. derived the quantum trajectory model. L.R.W., P.K., and M.S.S. provided supervision and expertise. N.J.M., D.H., L.B., and M.D. wrote the manuscript, with input from all authors. N.J.M. and D.H. contributed equally to this work.

Disclosures. The authors declare no conflicts of interest.

Data availability. Data underlying the results presented in this paper are not publicly available at this time but can be obtained from the authors on reasonable request.

Supplemental document. See Supplement 1 for supporting content.

REFERENCES

1. N. O. Antoniadis, N. Tomm, T. Jakubczyk, *et al.*, "A chiral one-dimensional atom using a quantum dot in an open microcavity," npj Quantum Inf. **8**, 27 (2022).
2. F. Liu, A. J. Brash, J. O'Hara, *et al.*, "High Purcell factor generation of indistinguishable on-chip single photons," Nat. Nanotechnol. **13**, 835–840 (2018).
3. M. J. Mehrabad, A. P. Foster, N. J. Martin, *et al.*, "Chiral topological add–drop filter for integrated quantum photonic circuits," Optica **10**, 415–421 (2023).
4. P. Lodahl, A. Floris van Driel, I. S. Nikolaev, *et al.*, "Controlling the dynamics of spontaneous emission from quantum dots by photonic crystals," Nature **430**, 654–657 (2004).
5. W. Fang, Y. Chen, Y. Zeng, *et al.*, "Anisotropic mode excitations and enhanced quantum interference in quantum emitter-metasurface coupled systems," New J. Phys. **24**, 093006 (2022).
6. J. Volz, M. Scheucher, C. Junge, *et al.*, "Nonlinear phase shift for single fibre-guided photons interacting with a single resonator-enhanced atom," Nat. Photonics **8**, 965–970 (2014).
7. F. Najafi, J. Mower, N. C. Harris, *et al.*, "On-chip detection of non-classical light by scalable integration of single-photon detectors," Nat. Commun. **6**, 5873 (2015).
8. S. Gyger, J. Zichi, L. Schweickert, *et al.*, "Reconfigurable photonics with on-chip single-photon detectors," Nat. Commun. **12**, 1408 (2021).
9. M. Arcari, I. Söllner, A. Javadi, *et al.*, "Near-unity coupling efficiency of a quantum emitter to a photonic crystal waveguide," Phys. Rev. Lett. **113**, 093603 (2014).
10. M.-A. Lemonde, S. Meesala, A. Sipahigil, *et al.*, "Phonon networks with silicon-vacancy centers in diamond waveguides," Phys. Rev. Lett. **120**, 213603 (2018).
11. X. Zhou, H. Tamura, T.-H. Chang, *et al.*, "Coupling single atoms to a nanophotonic whispering-gallery-mode resonator via optical guiding," Phys. Rev. Lett. **130**, 103601 (2023).
12. E. M. Purcell, H. C. Torrey, and R. V. Pound, "Resonance absorption by nuclear magnetic moments in a solid," Phys. Rev. **69**, 37 (1946).
13. D. Englund, D. Fattal, E. Waks, *et al.*, "Controlling the spontaneous emission rate of single quantum dots in a two-dimensional photonic crystal," Phys. Rev. Lett. **95**, 013904 (2005).
14. M. Duda, L. Brunswick, L. R. Wilson, *et al.*, "Efficient, high-fidelity single-photon switch based on waveguide-coupled cavities," Phys. Rev. A **110**, 042615 (2024).
15. C. P. Dietrich, A. Fiore, M. G. Thompson, *et al.*, "GaAs integrated quantum photonics: towards compact and multi-functional quantum photonic integrated circuits," Laser Photonics Rev. **10**, 870–894 (2016).
16. R. J. Coles, D. M. Price, J. E. Dixon, *et al.*, "Chirality of nanophotonic waveguide with embedded quantum emitter for unidirectional spin transfer," Nat. Commun. **7**, 11183 (2016).
17. R. J. Coles, D. M. Price, B. Royall, *et al.*, "Path-dependent initialization of a single quantum dot exciton spin in a nanophotonic waveguide," Phys. Rev. B **95**, 121401(R) (2017).
18. C. Gonzalez-Ballestero, A. Gonzalez-Tudela, F. J. Garcia-Vidal, *et al.*, "Chiral route to spontaneous entanglement generation," Phys. Rev. B **92**, 155304 (2015).
19. M. Scheucher, A. Hilico, E. Will, *et al.*, "Quantum optical circulator controlled by a single chirally coupled atom," Science **354**, 1577–1580 (2016).
20. S. Mahmoodian, K. Prindal-Nielsen, I. Söllner, *et al.*, "Engineering chiral light–matter interaction in photonic crystal waveguides with slow light," Opt. Mater. Express **7**, 43–51 (2017).
21. H. Siampour, C. O'Rourke, A. J. Brash, *et al.*, "Observation of large spontaneous emission rate enhancement of quantum dots in a broken-symmetry slow-light waveguide," npj Quantum Inf. **9**, 15 (2023).
22. N. J. Martin, M. Jalali Mehrabad, X. Chen, *et al.*, "Topological and conventional nanophotonic waveguides for directional integrated quantum optics," Phys. Rev. Res. **6**, L022065 (2024).
23. L. Hallacy, N. J. Martin, M. J. Mehrabad, *et al.*, "Nonlinear quantum optics at a topological interface enabled by defect engineering," npj Nanophotonics **2**, 9 (2025).
24. D. Hallett, A. P. Foster, D. Whittaker, *et al.*, "Engineering chiral light–matter interactions in a waveguide-coupled nanocavity," ACS Photonics **9**, 706–713 (2022).
25. C. W. Gardiner and M. J. Collett, "Input and output in damped quantum systems: quantum stochastic differential equations and the master equation," Phys. Rev. A **31**, 3761 (1985).
26. S. Fan, Ş. E. Kocabaş, and J.-T. Shen, "Input-output formalism for few-photon transport in one-dimensional nanophotonic waveguides coupled to a qubit," Phys. Rev. A **82**, 063821 (2010).
27. L. Tian and H. J. Carmichael, "Quantum trajectory simulations of two-state behavior in an optical cavity containing one atom," Phys. Rev. A **46**, R6801(R) (1992).
28. S. A. Regidor, G. Crowder, H. Carmichael, *et al.*, "Modeling quantum light-matter interactions in waveguide QED with retardation, nonlinear interactions, and a time-delayed feedback: matrix product states versus a space-discretized waveguide model," Phys. Rev. Res. **3**, 023030 (2021).
29. G. Crowder, L. Ramunno, and S. Hughes, "Quantum trajectory theory and simulations of nonlinear spectra and multiphoton effects in waveguide-QED systems with a time-delayed coherent feedback," Phys. Rev. A **106**, 013714 (2022).
30. S. Barik, A. Karasahin, S. Mittal, *et al.*, "Chiral quantum optics using a topological resonator," Phys. Rev. B **101**, 205303 (2020).
31. M. J. Mehrabad, A. P. Foster, R. Dost, *et al.*, "Chiral topological photonics with an embedded quantum emitter," Optica **7**, 1690–1696 (2020).
32. A. Javadi, D. Ding, M. H. Appel, *et al.*, "Spin–photon interface and spin-controlled photon switching in a nanobeam waveguide," Nat. Nanotechnol. **13**, 398–403 (2018).
33. C. Bentham, I. E. Itskevich, R. J. Coles, *et al.*, "On-chip electrically controlled routing of photons from a single quantum dot," Appl. Phys. Lett. **106**, 221101 (2015).
34. L. Sapienza, M. Davanço, A. Badolato, *et al.*, "Nanoscale optical positioning of single quantum dots for bright and pure single-photon emission," Nat. Commun. **6**, 7833 (2015).
35. I. J. Luxmoore, E. D. Ahmadi, B. J. Luxmoore, *et al.*, "Restoring mode degeneracy in H1 photonic crystal cavities by uniaxial strain tuning," Appl. Phys. Lett. **100**, 121116 (2012).
36. M. Bundgaard-Nielsen, D. Englund, M. Heuck, *et al.*, "WaveguideQED.jl: an efficient framework for simulating non-Markovian waveguide quantum electrodynamics," Quantum **9**, 1710 (2025).
37. H. Wang, Y.-M. He, T.-H. Chung, *et al.*, "Towards optimal single-photon sources from polarized microcavities," Nat. Photonics **13**, 770–775 (2019).
38. C. L. Phillips, A. J. Brash, M. Godsland, *et al.*, "Purcell-enhanced single photons at telecom wavelengths from a quantum dot in a photonic crystal cavity," Sci. Rep. **14**, 4450 (2024).
39. J.-H. Kim, T. Cai, C. J. K. Richardson, *et al.*, "Two-photon interference from a bright single-photon source at telecom wavelengths," Optica **3**, 577–584 (2016).
40. A. McCaw, J. Ewaniuk, B. J. Shastri, *et al.*, "Reconfigurable quantum photonic circuits based on quantum dots," Nanophotonics **13**, 2951–2959 (2024).
41. H. J. Kimble, "The quantum internet," Nature **453**, 1023–1030 (2008).